

A Miniaturized Electron Beam Column Simulation by the Fast Moving Least Square Reproducing Kernel Point Collocation Method

Do Wan KIM, Yongsik KIM¹, Young Chul KIM, Ho Seob KIM, Seungjoon AHN,
Yoon Young PARK² and Dae-Wook KIM

*Division of Natural Science/Center for Next Generation Semiconductor Technology, Sun Moon University,
100 Kalsan-ri, Tangjeong-myeon, Asan-si, Chung-nam 336-708, Republic of Korea*

¹*Department of Mathematics, Yonsei University, Seoul 120-749, Republic of Korea*

²*Division of Computer and Information Science, Sun Moon University,
100 Kalsan-ri, Tangjeong-myeon, Asan-si, Chung-nam 336-708, Republic of Korea*

(Received November 18, 2002; revised manuscript received January 27, 2003; accepted for publication January 27, 2003)

A miniaturized electron beam column, microcolumn, operated at a low electron energy of 1–2 keV has been simulated by the fast moving least square reproducing kernel point collocation method (FCM) which is a new concept of point collocation calculations. The salient feature of the method here is the use of the dilation function instead of constant dilation parameter. The simulation results of FCM for microcolumn configuration show good agreement with previous calculation and experimental results. Typically, the electron beam column design has been simulated by the finite difference method (FDM) with the grid and finite element method (FEM) based on mesh generation. However, The FCM method dilation function can readily calculate high-aspect-ratio structures employing only nodes instead of grid or mesh generation. The accuracy of this method will be proved through careful analysis of the error between numerical and analytic solutions. The full microcolumn structure consisting of electron emitter, source lens, and Einzel lens parts can be readily calculated by FCM. We will discuss the basic concept of FCM and its applications in this paper. [DOI: 10.1143/JJAP.42.3842]

KEYWORDS: FMLSrk method, dilation function, electrostatic microcolumn, point collocation scheme, computational methodology, electron beam

1. Introduction

The potentials and fields in the electrostatic and magnetic lens system are usually computed by the first-order finite element method (FEM) and/or finite difference method (FDM). In these methods, the mesh generation for the problems of complicated geometries is not simple. From this viewpoint, the meshfree method is appealing because it does not require mesh generation. Since the pioneering work on the meshfree method, smoothed particle hydrodynamics (SPH),¹⁾ several meshfree methods such as the diffuse element method (DEM),²⁾ element free Galerkin method (EFG),³⁾ moving least square reproducing kernel method (MLSrk),⁴⁾ and meshless point collocation method⁵⁾ have been proposed. EFG has been widely used and its successful implementations have been reported,^{6–8)} although this method uses background cells. Additionally, the coupling of the point collocation method and meshfree method which is called the meshfree point collocation method (MPCM)^{5,9,10)} has been investigated and it exhibited reliability. The applications of the meshfree method for electromagnetic field computation have been reported.^{11,12)} Recently, a new approximation method called the fast moving least square reproducing kernel method (FMLSrk)¹³⁾ has been proposed. In this method, the values of shape functions and the values of all its approximated derivatives are calculated simultaneously. Based on these approximations, we proposed point collocation schemes to solve the numerical solutions of partial differential equations. The details of the methodologies and numerical examples such as Poisson and Stokes problems can be found in ref. 13. This point collocation scheme using the FMLSrk method is fast and convenient, since it neither calculates the derivatives separately nor does it require mesh generation. Therefore, we have tried to apply this method to some physical problems, especially to the electrostatic microcolumn sys-

tem. However, in this case, the domain of the problem is nearly singular and has multi-scales. For instance, there are sharp edges of columns and an extremely small region concerned with the electron emitter. In the previous paper, such a situation has not been considered. Hence, we require an improved point collocation scheme for concentrated nodes in the small-scale region. This is why we adapt the dilation function instead of constant dilation parameter. This is not only the main emphasis point but also a distinct contribution from the previous work.

The microcolumn system has been studied experimentally and has attracted considerable interest because of its potential applications as a miniaturized electron source and its use in various types of equipment based on it.^{14,15)} In this work, we will discuss the basic concept of fast moving least square reproducing kernel point collocation method (FCM) and its applications to the microcolumn system as well as a numerical analysis on the validity of this method.

2. Fast Moving Least Square Reproducing Kernel Approximation

In this section, the brief summary of FMLSrk is described for the understanding of this numerical method. However, the intrinsic properties of the FMLSrk method in the theorem at the end of this section are preserved although the dilation parameter ρ below is replaced with a positive continuous function ρ_x . Thus we introduced the FMLSrk methodology briefly.

Let Ω be a bounded domain in \mathbb{R}^n and $u(x)$ be a continuous function defined in $\Omega \subset \mathbb{R}^n$. We also let $\Lambda = \{x_I \in \overline{\Omega} | I = 1, \dots, NP\}$ be a set of distributed nodes both in Ω and on its boundary. Throughout this paper, multi-index notations are employed. When $\alpha = (\alpha_1, \dots, \alpha_n)$ is an n -tuple of nonnegative integers and $x = (x_1, x_2, \dots, x_n) \in \mathbb{R}^n$, we define

$$\begin{aligned}
 |\alpha| &\equiv \sum_{i=1}^n \alpha_i, \\
 \alpha! &\equiv \alpha_1! \alpha_2! \cdots \alpha_n!, \\
 \mathbf{x}^\alpha &\equiv x_1^{\alpha_1} x_2^{\alpha_2} \cdots x_n^{\alpha_n},
 \end{aligned} \tag{2.1}$$

and write the α -th derivative of a smooth function as

$$D_{\mathbf{x}}^\alpha \equiv \partial_{x_1}^{\alpha_1} \partial_{x_2}^{\alpha_2} \cdots \partial_{x_n}^{\alpha_n}.$$

Now let us introduce the vector of complete basis polynomials in \mathbb{R}^n of the order less than or equal to m such that

$$\mathbf{P}_m(\mathbf{x}) = (\mathbf{x}^{\beta_1}, \mathbf{x}^{\beta_2}, \dots, \mathbf{x}^{\beta_L})^T \in \mathbb{R}^{\frac{(n+m)!}{n!m!}}, \tag{2.2}$$

where β_k 's are all multi-indices of n -tuples in lexicographical order. For example, if $n = 2$ and $m = 2$, then the multi-indices are arranged in the order of $(0,0), (1,0), (0,1), (2,0), (1,1)$ and $(0,2)$, and thus $\mathbf{P}_m(\mathbf{x})$ is $(1, x, y, x^2, xy, y^2)^T$. The dimension of $\mathbf{P}_m(\mathbf{x})$ is obviously $(n+m)!/n!m!$.

What we want to do first is to determine the best local approximation of $u(\mathbf{x})$ at $\bar{\mathbf{x}} \in \bar{\Omega}$ of the following form

$$U_m(\mathbf{x}, \bar{\mathbf{x}}) = \mathbf{P}_m\left(\frac{\mathbf{x} - \bar{\mathbf{x}}}{\rho}\right) \cdot \mathbf{a}(\bar{\mathbf{x}}) = \mathbf{P}_m^T\left(\frac{\mathbf{x} - \bar{\mathbf{x}}}{\rho}\right) \mathbf{a}(\bar{\mathbf{x}}), \tag{2.3}$$

in the manner of minimizing the locally weighted square functional

$$J(\mathbf{a}(\bar{\mathbf{x}})) \equiv \sum_{\mathbf{x}_I \in \Lambda} |u(\mathbf{x}_I) - U_m(\mathbf{x}_I, \bar{\mathbf{x}})|^2 \Phi\left(\frac{\mathbf{x}_I - \bar{\mathbf{x}}}{\rho}\right), \tag{2.4}$$

where $\Phi(\mathbf{y})$ is nonnegative and compactly supported continuous function in \mathbb{R}^n the so called window function. The minimizing procedure yields the best local approximation of $u(\mathbf{x})$ at $\bar{\mathbf{x}}$

$$\begin{aligned}
 U_m(\mathbf{x}, \bar{\mathbf{x}}) &= \mathbf{P}_m^T\left(\frac{\mathbf{x} - \bar{\mathbf{x}}}{\rho}\right) \\
 &\quad \sum_{\mathbf{x}_I \in \Lambda} M^{-1}(\bar{\mathbf{x}}) \mathbf{P}_m\left(\frac{\mathbf{x}_I - \bar{\mathbf{x}}}{\rho}\right) \Phi\left(\frac{\mathbf{x}_I - \bar{\mathbf{x}}}{\rho}\right) u(\mathbf{x}_I),
 \end{aligned} \tag{2.5}$$

where $M(\bar{\mathbf{x}})$ is the moment matrix defined by

$$M(\bar{\mathbf{x}}) \equiv \sum_{\mathbf{x}_I \in \Lambda} \mathbf{P}_m\left(\frac{\mathbf{x}_I - \bar{\mathbf{x}}}{\rho}\right) \mathbf{P}_m^T\left(\frac{\mathbf{x}_I - \bar{\mathbf{x}}}{\rho}\right) \Phi\left(\frac{\mathbf{x}_I - \bar{\mathbf{x}}}{\rho}\right). \tag{2.6}$$

Based on the best local approximation $U(\mathbf{x}, \bar{\mathbf{x}})$, the locally approximated derivatives of $u(\mathbf{x})$ are defined by

$$\begin{aligned}
 D_{\mathbf{x}}^\alpha U_m(\mathbf{x}, \bar{\mathbf{x}}) &= \left[D_{\mathbf{x}}^\alpha \mathbf{P}_m^T\left(\frac{\mathbf{x} - \bar{\mathbf{x}}}{\rho}\right) \right] \\
 &\quad \sum_{\mathbf{x}_I \in \Lambda} M^{-1}(\bar{\mathbf{x}}) \mathbf{P}_m\left(\frac{\mathbf{x}_I - \bar{\mathbf{x}}}{\rho}\right) \Phi\left(\frac{\mathbf{x}_I - \bar{\mathbf{x}}}{\rho}\right) u(\mathbf{x}_I),
 \end{aligned} \tag{2.7}$$

where $|\alpha| \leq m$. We arrive at the position where the global approximations of all derivatives of $u(\mathbf{x})$ are derived from the local ones of eq. (2.7) simply by taking the limit as $\bar{\mathbf{x}}$ tends to \mathbf{x} . Thus we define notations of the global approximations of $u(\mathbf{x})$ and obtain the identities

$$\begin{aligned}
 D_m^{h,\alpha} u(\mathbf{x}) &\equiv \lim_{\bar{\mathbf{x}} \rightarrow \mathbf{x}} D_{\mathbf{x}}^\alpha U_m(\mathbf{x}, \bar{\mathbf{x}}) \\
 &= \sum_{\mathbf{x}_I \in \Lambda} \Psi_I^{[\alpha]}(\mathbf{x}) u(\mathbf{x}_I),
 \end{aligned} \tag{2.8}$$

where $|\alpha| \leq m$ and the functions $\Psi_I^{[\alpha]}(\mathbf{x})$'s are defined as the solution of the following matrix equation

$$M(\mathbf{x}) \begin{pmatrix} \frac{\rho^{|\beta_1|}}{\beta_1!} \Psi_I^{[\beta_1]}(\mathbf{x}) \\ \frac{\rho^{|\beta_2|}}{\beta_2!} \Psi_I^{[\beta_2]}(\mathbf{x}) \\ \vdots \\ \frac{\rho^{|\beta_L|}}{\beta_L!} \Psi_I^{[\beta_L]}(\mathbf{x}) \end{pmatrix} = P_m\left(\frac{\mathbf{x}_I - \mathbf{x}}{\rho}\right) \Phi\left(\frac{\mathbf{x}_I - \mathbf{x}}{\rho}\right), \tag{2.9}$$

where β_k 's are multi-indices and $|\beta_k| \leq m$ and $\mathbf{x}_I \in \Lambda$. We call $\Psi_I^{[\alpha]}(\mathbf{x})$ the α -th shape function associated with the window function Φ , or briefly call it the α -th shape function if there is no confusion. Note that, $\Psi_I^{[0]}(\mathbf{x})$'s are standard shape functions of meshfree methods.

Theorem 2.1. (*Properties of FMLSrk*)

- (1) (*Generalized m -th order consistency*) Suppose that $u(\mathbf{x})$ is a polynomial of the order less than or equal to m . Then the interpolation operator $D_m^{h,\alpha}$ produces $D^\alpha u(\mathbf{x})$, i.e.,

$$D_m^{h,\alpha} u(\mathbf{x}) = D^\alpha u(\mathbf{x}) \tag{2.10}$$

for any α , $|\alpha| \leq m$.

- (2) (*Truncation error for approximated derivatives*) Assume the window function $\Phi(\mathbf{x}) \in C_0^0(\mathbb{R}^n)$ and $v(\mathbf{x}) \in C^{m+1}(\Omega)$, where Ω is a bounded open set in \mathbb{R}^n . Let Λ be a node set on which any moment matrix $M(\mathbf{x})$ for $\mathbf{x} \in \bar{\Omega}$ is assumed to be invertible for some dilation parameter $\rho > 0$. Suppose the boundary of Ω is smooth and $\text{supp } \Psi_I^{[0]} \cap \bar{\Omega}$ is convex for each I .

If m and p satisfy

$$m > \frac{n}{p} - 1, \tag{2.11}$$

then the following estimate holds

$$\|D_m^{h,\beta} v - D_m^{h,\beta} v\|_{L^p(\Omega)} \leq C(m) \rho^{m+1-|\beta|} \|v\|_{W^{m+1,p}(\Omega)}, \tag{2.12}$$

for all β , $|\beta| \leq m$.

3. Point Collocation Scheme Based on FMLSrk Approximation

We will propose a point collocation scheme from a general point of view. In order to obtain the meshfree numerical solution of a partial differential equation, we first interpolate the solution $u(\mathbf{x})$ of the partial differential equation such that

$$D_m^{h,0} u = \sum_{\mathbf{x}_I \in \Lambda} u_I \Psi_I^{[0]}(\mathbf{x}) \tag{3.1}$$

where u_I should be determined later from the governing equations. Then the approximation theorem 1 allows us to approximate the derivatives of $u(\mathbf{x})$ in the partial differential equations and on the boundary conditions such that

$$D_m^{h,\beta} u = \sum_{\mathbf{x}_I \in \Lambda} u_I \Psi_I^{[\beta]}(\mathbf{x}) \tag{3.2}$$

for $0 < |\beta| \leq m$. In the point collocation scheme, we preferably use the following type of window function

$$\Phi(\mathbf{y}) = \begin{cases} (1 - \|\mathbf{y}\|)^j, & \text{when } \|\mathbf{y}\| < 1, \quad j > 0, \\ 0, & \text{otherwise,} \end{cases} \quad (3.3)$$

which is not differentiable at $\mathbf{x} = \mathbf{0}$. We call j the power of the window function. Usually, we take the case when $j = 4$ for the second order partial differential equations.

In order to expose a point collocation scheme, we consider the Poisson problem

$$-\Delta u = f, \quad \text{in } \Omega \quad (3.4)$$

$$u = g, \quad \text{on } \Gamma_D \quad (3.5)$$

$$\frac{\partial u}{\partial n} = h, \quad \text{on } \Gamma_N \quad (3.6)$$

where $\partial\Omega = \Gamma_D \cup \Gamma_N$, $\Gamma_D \cap \Gamma_N = \phi$. We propose the point collocation discretization of the above Poisson problem using the approximations (3.13) and (3.14) as

$$U(\mathbf{x}) = \sum_{\mathbf{x}_j \in \Lambda} u_j \Psi_j^{(0,0)}(\mathbf{x}), \quad (3.7)$$

$$-\sum_{\mathbf{x}_j \in \Lambda} u_j (\Psi_j^{(2,0)}(\mathbf{x}^i) + \Psi_j^{(0,2)}(\mathbf{x}^i)) = f(\mathbf{x}^i),$$

$$\sum_{\mathbf{x}_j \in \Lambda} u_j \Psi_j^{(0,0)}(\mathbf{x}^d) = g(\mathbf{x}^d),$$

$$\sum_{\mathbf{x}_j \in \Lambda} u_j (\Psi_j^{(1,0)}(\mathbf{x}^n), \Psi_j^{(0,1)}(\mathbf{x}^n)) \cdot \mathbf{n}(\mathbf{x}^n) = h(\mathbf{x}^n), \quad (3.8)$$

$$\mathbf{x}^i \in \Lambda_i, \quad \mathbf{x}^d \in \Lambda_d, \quad \mathbf{x}^n \in \Lambda_n, \quad (3.9)$$

where $\Lambda = \Lambda_i \cup \Lambda_d \cup \Lambda_n$, and Λ_i , Λ_d and Λ_n are sets of interior nodes, Dirichlet boundary nodes and Neumann boundary nodes, respectively. Here $\mathbf{n}(\mathbf{x}^n)$ is the outward unit normal vector at $\mathbf{x}^n \in \Lambda_n$. In this case, the second order approximated derivatives are needed. Thus, we choose the order m of basis polynomial P_m greater than or equal to 2.

It is worth noting that the extension of the above method using a positive dilation function is considerably natural. The constant dilation parameter ρ can be replaced with the continuous dilation function ρ_x . Of course, in this case, all shape functions depend on ρ_x . It can be proved that it is possible to introduce ρ_x with the generalized m -th order consistency condition preserved in FMLSrk approximation. Unless the dilation function ρ_x is differentiable, other meshfree methods fail to calculate the derivatives of shape functions. For the preconditioning, we propose an improved scheme for concentrated nodes as

$$-\sum_{\mathbf{x}_j \in \Lambda} u_j \rho_{x^i}^2 (\Psi_j^{(2,0)}(\mathbf{x}^i) + \Psi_j^{(0,2)}(\mathbf{x}^i)) = \rho_{x^i}^2 f(\mathbf{x}^i), \quad (3.10)$$

$$\sum_{\mathbf{x}_j \in \Lambda} u_j \Psi_j^{(0,0)}(\mathbf{x}^d) = g(\mathbf{x}^d), \quad (3.11)$$

$$\sum_{\mathbf{x}_j \in \Lambda} u_j \rho_{x^n} (\Psi_j^{(1,0)}(\mathbf{x}^n), \Psi_j^{(0,1)}(\mathbf{x}^n)) \cdot \mathbf{n}(\mathbf{x}^n) = \rho_{x^n} h(\mathbf{x}^n), \quad (3.12)$$

$$\mathbf{x}^i \in \Lambda_i, \quad \mathbf{x}^d \in \Lambda_d, \quad \mathbf{x}^n \in \Lambda_n.$$

4. Numerical Simulations

As already described above, only the node configuration is necessary for the whole domain considered in this computa-

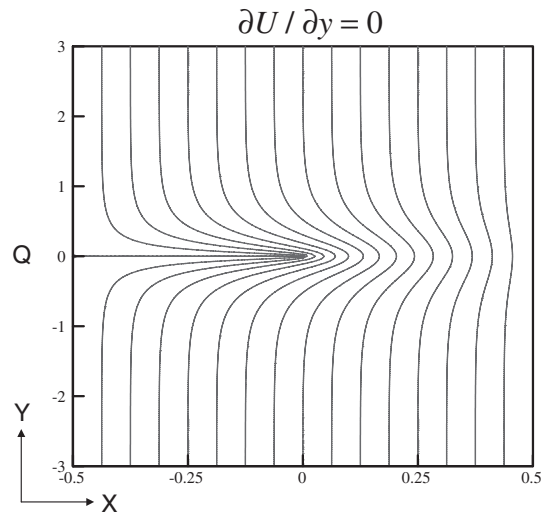


Fig. 1. Singular domain configuration of the potential flow in 2-dimensional pipe with a barrier inside. The solid lines indicate the numerically obtained solution with high density node set.

tion method. Thus, we have defined the domain as the whole area surrounded by the boundaries, either constant value boundaries (Dirichlet boundary condition) or constant derivative boundaries (Neumann boundary condition). The nodes with proper inter-distances and suitable for the geometry of each system were generated. In this work, all computation processes were performed based on 2-dimensional modelling as the concerned systems are cylindrically symmetric.

In order to check the reliability of this computational method, we have applied it to a sample system having an analytical solution. We have considered the potential flow problem in a 2-dimensional pipe with a barrier inside. The flow region Ω has a serious singularity of interior angle 2π as shown in Fig. 1 by solid lines

$$\Omega = \left\{ (x, y) \mid -\frac{1}{2} < x < \frac{1}{2} \right\} - D_b \quad (4.1)$$

where $D_b = \{-\frac{1}{2} \leq x \leq \frac{1}{2}, y = 0\}$. In the real numerical calculation, we restricted the infinite flow domain Ω to the truncated domain Ω^h such that $\Omega^h = \Omega \cap \{(x, y) \mid |y| < 3\}$. The governing equation is the Poisson equation with 0 forcing term, i.e., the harmonic equation in the singular domain.

$$-\Delta u = 0, \quad \text{in } \Omega^h \quad (4.2)$$

$u(x, y) = Q$, on $x = -\frac{1}{2}$ or $-\frac{1}{2} < x \leq 0$, $y = 0$ and, $u(x, y) = 0$, on $x = \frac{1}{2}$, where, Q is the potential value at the boundary i.e., Dirichlet boundary condition. The exact solution on Ω is

$$u(z) = \Im \frac{Q}{\pi} \log[2 \sin \pi z - 1 + i(1 - (2 \sin \pi z - 1)^2)^{\frac{1}{2}}], \quad (4.3)$$

$$z = x + iy$$

where the imaginary symbol \Im indicates the imaginary part of the complex valued function and the logarithm has the principal argument $-\pi < \theta < \pi$. In Fig. 1, the equipotential lines obtained numerically are indicated by solid lines. Hereafter, the analytic solution will be abbreviated as u_s and

the numerically obtained ones as U_s

In the process of numerical calculation, the Dirichlet boundary value was set to be $Q = 5$. The physical situation corresponding to this mathematical condition is that the voltage applied to the left plate and the slit is 5 V and the right plate is grounded. Additionally, the assumed Neumann boundary condition of $\partial U/\partial y = 0$, is applied on $y = \pm 3$ as we do not know the exact potential values and their gradients. Though we can calculate these values in this problem, they are not usually available at boundaries. However, even in a real system, we can guess that the gradient of the potential would be zero in the region far from the slit, that is $(\partial u/\partial y)|_{\pm\infty} = 0$.

Numerical calculation was performed using two different sets of nodes.: (i) In the first set, the node number density is relatively low and the distance between the neighboring node points along the x - or y -direction was set to be $\delta x = 0.002$ and $\delta y = 0.006$. (ii) In the second set, the node number density was increased so that inter-node distance was just half of that in the first set, $\delta x = 0.001$ and $\delta y = 0.003$. Therefore, the total number of nodes in the high density node set is four times as large as that in the low density case. The feature of the numerical solution obtained with a high density node set is presented in Fig. 1 by solid lines. The difference between the analytic and numerical solutions was obtained at each node point. The average value of the relative error, i.e., $\bar{D} = \frac{1}{n} \sum D(i)$ was 0.0005 and 0.0002 for low and high density nodes, respectively. Here, n is the total number of nodes in each configuration and $D(i)$ is defined as $D(i) = |U_s(i) - u_s(i)|/|u_s(i)|$ at i -th node point. The value of \bar{D} is thought to be sufficiently small for usual numerical methods. Also, the L^2 -error is measured as

$$L^2 - \text{error} \equiv \|u_s - U_s\| \equiv \left[\frac{\sum |u_s(X_I) - U_s(X_I)|^2}{\sum |u_s(X_I)|^2} \right]^{1/2} \quad (4.4)$$

As expected, L^2 -error was reduced with the increase of the node number; 0.0006 for low and 0.0003 for high density node sets.

The sectional views of numerical solutions were compared with analytic ones along several typical lines in the domain. In Fig. 2(a), solid lines indicate the analytic solution and discrete symbols indicate numerically estimated solutions obtained with a low-density node set along the lines of $y = \text{constant}$; Circles, squares, up-triangles, and down-triangles indicate numerically obtained values along $y = 0, y = 0.06, y = 0.24,$ and $y = 2.52,$ respectively. These plots suggest that numerically obtained solutions agree quite well with the exact ones even in the case of a low-density node set.

In order to illustrate the accuracy variation quantitatively, we have plotted the sectional view of relative error, $D(i)$, along the same lines as in Fig. 2(b). At the origin, the relative error is around 0.022 which is much larger than those in other regions, which are less than 0.01. When numerical estimation is performed with a high-density node set, the error is reduced uniformly and the comparison between the errors in low and high density node sets is shown in Fig. 2(c). Along the direction parallel to the y axis, we have examined several typical lines such as $x = -0.4, -0.06, 0.00, 0.06,$ and $0.3,$ and the resulting errors were less

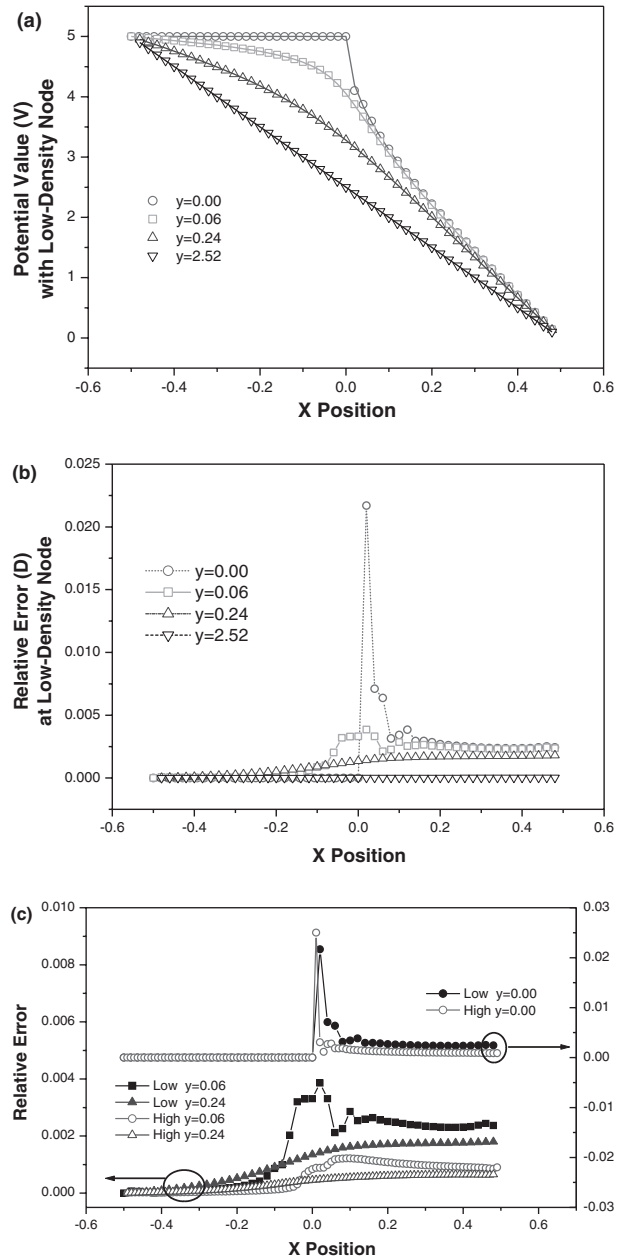


Fig. 2. (a) Sectional views of the numerical and analytic solutions. The solid line indicates the analytic solution and circles, squares, up-triangles, and down-triangles indicate the numerically obtained solution along $y = 0, 0.06, 0.24,$ and $2.52,$ respectively. (b) Sectional view of relative error, $D(i)$, along the same lines. (c) Comparison of relative errors obtained with low (solid symbols) and high (open symbols) density node set.

than 0.004. The maximum error appears also at the origin. These results can be summarized as follows; i) the error is negligibly small in the region far from the singular structure i.e., the origin. Even in the region near the origin, the maximum relative error is less than 0.03. ii) The magnitude of error decreases uniformly over the entire domain with the increase of node density.

In this computation method, we do not differentiate the shape functions to obtain their derivatives but independently obtain them by treating the derivatives as another shape function. This is the main difference between this method and the conventional point collocation scheme, which makes it compulsory to clarify the validity of this approach. Though

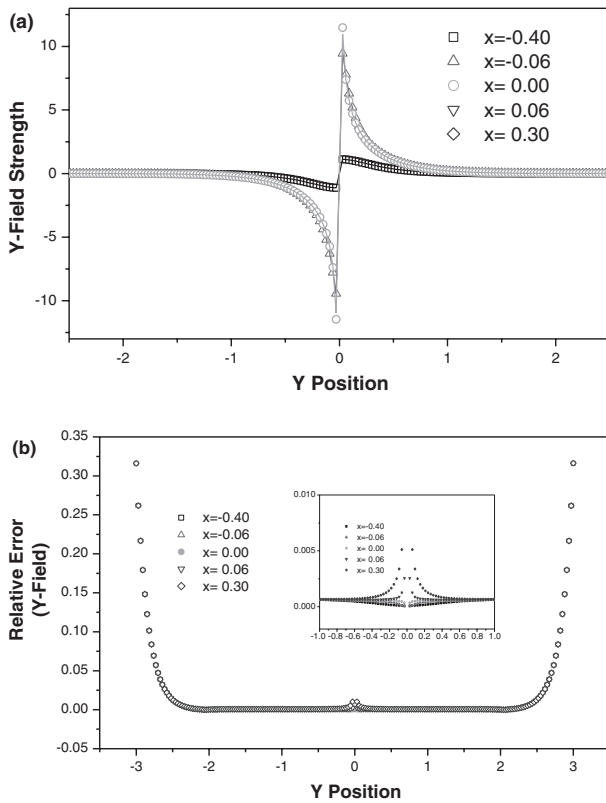


Fig. 3. (a) $-\partial U_s/\partial y$ along $x = -0.4, -0.06, 0.00, 0.06,$ and 0.3 lines. Squares, circles, up-triangles, down triangles and diamonds indicate numerically estimated values of $-\partial U_s/\partial y$ along $x = -0.4, -0.06, 0.00, 0.06,$ and 0.3 lines, respectively. Solid lines indicate analytic values. (b) Relative error between $-\partial U_s/\partial y$ and $-\partial u_s/\partial y$.

it is proved mathematically in ref. 13, we tried to check it by plotting the field strengths, both $-\partial U_s/\partial x$ (X -field strength) and $-\partial U_s/\partial y$ (Y -field strength), along the same lines traced in Fig. 2.

Along the lines parallel to the x axis, $-\partial U_s/\partial y$ varies gradually and does not show any abrupt behavior, which is not shown here. In addition, the magnitude of the relative error is less than 0.015 for the whole domain. Figure 3(a) shows $-\partial U_s/\partial y$ along a few $x = \text{constant}$ lines, $x = -0.4, -0.06, 0.00, 0.06,$ and 0.3 . When $x \leq 0$, both $-\partial U_s/\partial y$ and $-\partial u_s/\partial y$ change abruptly when passing through $y = 0$ due to the slit (see the squares, circles, and up-triangles in the figure). It changes gradually, when $x > 0$ (see the down-triangles and diamonds in this figure). The solid lines indicate analytically obtained values of $-\partial u_s/\partial y$. Figure 3(b) shows the corresponding relative error between $-\partial U_s/\partial y$ and $-\partial u_s/\partial y$. The magnitude of error is less than 0.006 in most of the region, that is, $-2 < y < 2$, in this figure. However, when $y < -2.5$ or $y > 2.5$, the relative error increases rapidly and reaches 0.32 at $y = \pm 3$. This trend is the same for all the lines considered though there are slight differences near $y = 0$ as shown in the insert. At a glance, a relative error of 0.32 seems to be very large. However, it is important to remember that this large error did not originate from the methodology itself but from the boundary condition. For the convenience of numerical estimation, we have assigned the Neumann boundary condition of $-\partial U/\partial y = 0$ on $y = \pm 3$ instead of the exact analytic boundary condition of $-\partial u/\partial y = 0$ at $y = \pm \infty$. Therefore, $-\partial U/\partial y$ should

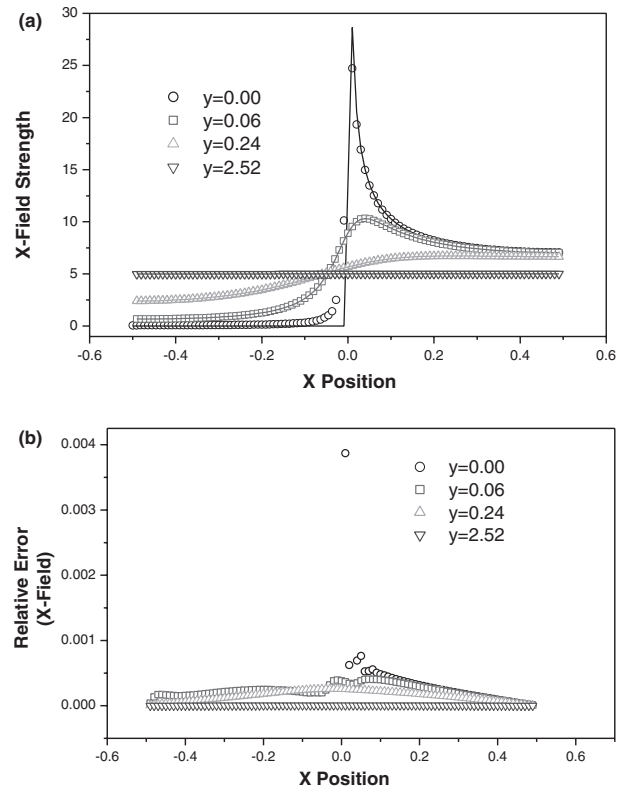


Fig. 4. (a) This figure presents $-\partial U_s/\partial x$ along the lines parallel to x -axis. The open circles, squares, up-triangles, and down-triangles represent $-\partial U_s/\partial x$'s along the lines of $y = 0.00, 0.06, 0.24,$ and 2.52 . (b) Relative errors between $-\partial U_s/\partial x$ and $-\partial u_s/\partial x$.

approach zero as $y \rightarrow \pm 3$ even though the real value is not zero. In other words, this large error did not originate from the computation method itself but from the roughly guessed boundary condition. We need to concentrate on the small error in the region of $-2 < y < 2$. Even though the forced error originating from the roughly taken boundary condition is ~ 0.3 , the error decreases rapidly to sufficiently small values, less than 0.006, as the node points recede from that boundary. This means that it is sufficient to determine the dimension of the whole domain several times larger than the size of the slit for obtaining a reasonable numerical solution.

Figure 4(a) presents $-\partial U_s/\partial x$ along a few lines parallel to the x -axis and (b) the corresponding relative error. In addition, owing to the existence of a singular point, the end of the slit, $-\partial U_s/\partial x$ shows an abrupt change at $x = 0$ if one follows $y = 0$. Along other lines, it varies smoothly. In this case, the relative error is also less than 0.001 except for the value of 0.004 at the origin. Along the lines parallel to the y -axis, $-\partial U_s/\partial x$ varies smoothly when $x > 0$. But when $x \leq 0$, it shows a singular change in its derivative (2nd derivative of potential) while satisfying the continuity of the tangential components of the electric field. The magnitude of relative error was proved to be less than 0.0006.

The error of $-\partial U_s/\partial x$ (maximum 0.001 except origin) is much smaller than that of $-\partial U_s/\partial y$ (maximum 0.015 except in the region near $y = \pm 3$). This is thought to be natural as the assigned Dirichlet boundary condition at the lines of $x = -1/2$ and $x = 1/2$ is not the guessed value but just the applied constant voltage. By the above assumptions, both the shape functions and their derivatives obtained simultaneous-

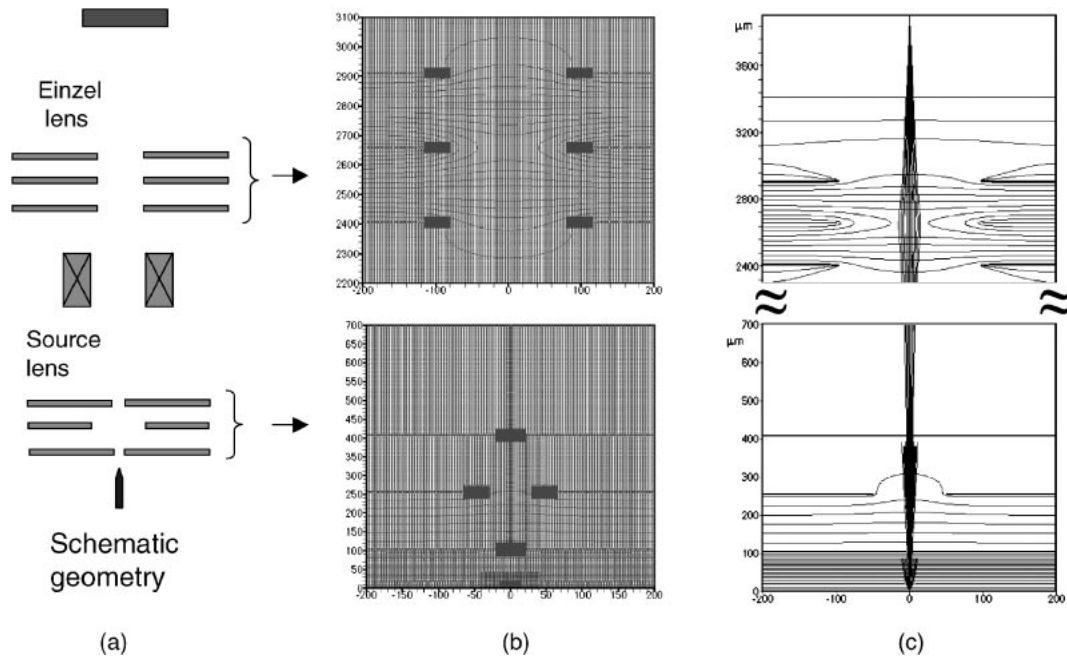


Fig. 5. (a) Schematic diagram of the microcolumn considered in this work. (b) The feature of gradually zoomed node configuration near tip and lens. Node density increases at the end of tip and lens. (c) Estimated potential and electron beam trajectory in the region of source and the Einzel lens.

ly by this method were proved to be acceptable as reasonable substitutes for real values.

The schematic diagram of the microcolumn considered in this work is shown in Fig. 5(a). In this diagram, the thickness of all the micro-electrostatic lenses is $2\mu\text{m}$. Above the electron emitter, the source lens system composed of three micro-electrostatic lenses is located. The spacings between the lenses are set to be $150\mu\text{m}$ and the aperture diameter is set to be 10, 100, and $10\mu\text{m}$, respectively from the bottom and followed by the deflector denoted by crossed rectangles. Finally, the Einzel lens system composed of three identical micro-electrostatic lenses in which the spacings between the lenses are set to be $250\mu\text{m}$ and the aperture diameter is $200\mu\text{m}$ is used and focuses the electron beam onto the sample shown as a horizontal rectangle.

The total length of this column is around 4 mm while the thickness of the composing lens is usually $2\mu\text{m}$ and the radius of the circular aperture ranges from a few to $200\mu\text{m}$ and the emitter width is less than $1\mu\text{m}$. The aspect ratio, the dimensional ratio between the largest and the smallest structure, of this system is around 4000, which is regarded as very large for the usual numerical calculation methods. Therefore, in order to save computation time for numerical estimation, gradual zooming is introduced. That is, the node configuration was generated such that the inter-node distance decreases by steps while approaching the fine structures such as the emitter tip or the end of the lens to avoid a rapid change of node distance which may result in an error during numerical estimation. This situation is well expressed in Fig. 5(b) which shows the gradually zoomed node configuration near the tip and lens.

Here, the concept of characteristic radius is introduced during the computation process. Characteristic radius is defined as the radius of the circular disk (or sphere in 3-dimensional case) having a characteristic number of node

points centered at the concerned node point during the computation. The estimated values at a certain node point, whether they are shape functions or their derivatives, are compared with those at the node points within that characteristic volume element. Therefore, characteristic radius varies according to node density. In this example, the characteristic radius in the main domain was taken to be less than $10\mu\text{m}$ and those in the zoomed regions are reduced by steps with the decrease of node distance. The strict meaning of aspect ratio is the ratio of the longest characteristic radius to the shortest one.

For the numerical calculation, we have assigned some boundary conditions; between the cathode (the bottom plate and emitter) and anode (the extractor lens) a constant potential difference of 1,000 was assigned depending on the electron energy. At the center electrode of Einzel lens, decelerating or accelerating voltage was assigned according to the operating mode. For the boundaries at the two vertical sides, the boundary condition of zero electric field, that is, $\partial V/\partial n = 0$ was applied. In Fig. 5(c), we have shown typical results such as estimated potential and electron beam trajectory, in the region of source and Einzel lens. The results of the other region are not displayed since electrons do not undergo significant acceleration because of the negligibly low potential and weak field.

For given values of parameters such as the dimension of each component and the boundary condition, the characteristics of the column including electrostatic potential inside column, corresponding field and electron motion will be determined. A typical example is shown in Fig. 6, the operation of the Einzel lens system depending on the voltage applied to the center electrode. Figure 6(a) shows the beam motion when the Einzel lens is operating in accelerating mode and Fig. 6(b) presents that in retarding mode. Similar results can be found in ref. 16. In order to certify that this

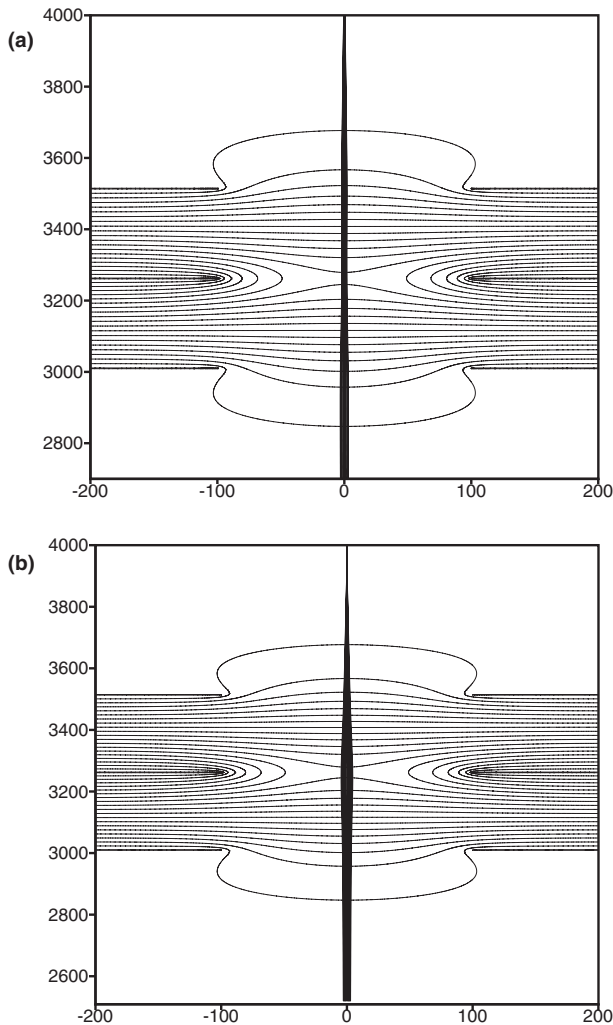


Fig. 6. Operation of the Einzel lens in (a) accelerating mode and (b) retarding mode.

method works well in a real full microcolumn structure, we have considered a system already reported.¹⁷⁾ The structure of the microcolumn considered in this work is exactly the same as that depicted in Fig. 5(a).

The spacings between the first lens and the second lens (the spacings between the second lens and the third lens in the source lens system were fixed to be $250\ \mu\text{m}$ ($600\ \mu\text{m}$) and the aperture diameter of the extractor (first lens of the source lens), center lens, and the limiting aperture was 5, 100, and $2.5\ \mu\text{m}$, respectively. The distance between the end of source lens and the first lens of the Einzel lens is taken to be $2050\ \mu\text{m}$, and the diameter of each Einzel lens and the spacing between them was set to be 200 and $250\ \mu\text{m}$, respectively. Here, the thicknesses of all the lenses were also set to be $2\ \mu\text{m}$. The operation of this system at 1 keV beam energy was simulated assuming that beam focusing is performed in retarding mode with the applied voltage of $-780\ \text{V}$, which is the same value used in the reference. The working distance and the beam diameter obtained through our simulation are 1.026 mm and 15.8 nm, respectively while those of the reference are 1.0 mm and 16 nm.

The above examples ensure that our point collocation scheme using the FMLSrk method is well applied for the

electrostatic field analysis in general electromagnetic systems and the optimization of vacuum microelectronic devices or microcolumn systems. As discussed above, the aspect ratio of a microcolumn system is very large and as far as the authors know, it is difficult to obtain a convergent solution in a self-consistent manner in such a high aspect ratio system. With this method, simply introducing a series of local zooming regions containing relatively fine geometries is sufficient for the convergency. Further detailed analysis on the full microcolumn operation based on changing the various parameters will be carried out.

5. Conclusion

A recently proposed computational methodology to solve numerical solutions of partial differential equations, the FCM was demonstrated and applied to the analysis of a miniaturized electron beam column. This method has merits such as easy applicability to high-aspect-ratio systems and convenient usage since it neither calculates the derivatives separately nor does it require mesh generation. Through error analysis of a system with a known analytic solution, both numerically obtained shape functions and their derivatives show excellent agreement with their analytic solutions. We applied FCM for the analysis of a microcolumn structure and obtained successful results compared with the previous report. This method can be applied to any arbitrary system regardless of its geometrical complexity and aspect ratio. Most of all, this method is accurate and very convenient as the mesh generation is not necessary, especially for 3-dimensional problems.

- 1) R. A. Gingold and J. J. Monaghan: *Monthly Notices Roy. Astronom. Soc.* **181** (1977) 275.
- 2) B. Nayroles, G. Touzot and P. Villon: *Comput. Mech.* **10** (1992) 307.
- 3) Y. Y. Lu, T. Belyschko and L. Gu: *Comput. Methods Appl. Mech. & Eng.* **113** (1994) 397.
- 4) W. K. Liu, S. Li and T. Belyschko: *Comput. Methods Appl. Mech. & Eng.* **143** (1996) 174.
- 5) N. R. Aluru: *Int. J. Numer. Methods Eng.* **47** (2000) 1083.
- 6) W. K. Liu, S. Jun, D. T. Sihling, Y. Chen and W. Hao: *Int. J. Numer. Methods Fluids* **24** (1997) 1391.
- 7) F. Gunther, W. K. Liw and D. Diachin: *Comput. Methods Appl. Mech. & Eng.* **190** (2000) 279.
- 8) H. J. Choe, D. W. Kim, H. H. Kim and Y. S. Kim: *Discrete & Continuous Dynamical Systems-Series B* **1** (2001) 495.
- 9) J. Furst and T. Sonar: *Z. Ang. Math. & Mech.* **81** (2001) 403.
- 10) X. Zhang, X. H. Liu, K. Z. Song and M. W. Lu: *Int. J. Numer. Methods Eng.* **51** (2001) 1089.
- 11) S. A. Viana and R. C. Mesquita: *IEEE Trans. Magn.* **35** (1999) 1372.
- 12) S. L. Ho, S. Yang, J. M. Machado and H. C. Wong: *IEEE Trans. Magn.* **37** (2001) 3198.
- 13) D. W. Kim and Y. Kim: *Int. J. Numer. Methods Eng.* **56** (2003) 1445.
- 14) T. H. P. Chang, M. G. R. Thomson, E. Kratschmer, H. S. Kim, M. L. Yu, K. Y. Lee, S. A. Rishton, B. W. Hussey and S. Zolgharnain: *J. Vac. Sci. Technol. B* **14** (1996) 3774.
- 15) T. H. P. Chang, M. G. R. Thomson, M. L. Yu, E. Kratschmer, H. S. Kim, K. Y. Lee, S. A. Rishton and S. Zolgharnain: *Microelectron. Eng.* **32** (1996) 113.
- 16) M. Sedlacek: *Electron Physics of Vacuum and Gaseous Devices* (John Wiley and Sons, 1996).
- 17) E. Kratschmer, H. S. Kim, M. G. R. Thomson, K. Y. Lee, S. A. Rishton, M. L. Yu and T. H. P. Chang: *J. Vac. Sci. Technol. B* **13** (1995) 2498.